PHYSICAL REVIEW B VOLUME 51, NUMBER 5 1 FEBRUARY 1995-I

Stacking-fault imaging using transmission ion channeling

P. J. C. King and M. B. H. Breese
Scanning Proton Microprobe Unit, Nuclear Physics Laboratory, University of Oxford, Keble Road, Oxford, OX1 3RH, United Kingdom

P. R. Wilshaw
Department of Materials, University of Oxford, Parks Road, Oxford, OX1 3PH, United Kingdom

G. W. Grime
Scanning Proton Microprobe Unit, Nuclear Physics Laboratory, University of Oxford, Keble Road, Oxford, OX1 3RH, United Kingdom

(Received 1 July 1994)

This paper gives a detailed analysis of the necessary conditions for observing stacking faults using transmission ion channeling. It is shown that transmission ion channeling images of individual stacking faults at least 10 μm below the surface of a 40-μm-thick silicon crystal can be produced by mapping the mean energy loss of channeled 3-MeV protons. The observed image contrast depends on whether axial or planar alignment is used and, in planar alignment, increases on going from $\{100\}$ to $\{110\}$ to $\{111\}$ planes. The criteria under which faults do not disturb the channeling process are considered. It is shown that for channeling in planes with reciprocal lattice vector **g**, faults with translation vector **R** are invisible if $\mathbf{g}\cdot\mathbf{R}$ is equal to zero or an integer. The use of backscattered rather than transmitted ions for image production is discussed.

I. INTRODUCTION

Ion channeling[1] is an established technique for the study of crystalline materials and enables the concentrations and depth distributions of crystal defects such as dislocations, stacking faults, and implantation damage to be determined. Such studies normally use backscattered ions produced by the interaction of a broad ion beam with the sample atoms and do not produce information on the spatial distribution of the defects. Recently, however, images of bunches of misfit dislocations[2,3] and individual misfit dislocations[4] in $\mathrm{Si}_{1-x}\mathrm{Ge}_x$/Si crystals have been produced using a focused ion beam from a nuclear microprobe by detecting ions transmitted through thinned samples. This technique is called channeling scanning transmission ion microscopy (CSTIM). Information on the nature of the dislocation bunches and their effects on the crystal lattice planes was deduced. It was also briefly demonstrated[4] that images of oxidation-induced stacking faults in a silicon crystal could be formed. This paper is a more detailed study of the ability of transmission ion channeling to image and characterize stacking faults.

II. ION CHANNELING

Channeling occurs when an ion beam is incident on a crystal parallel to a major axis of the crystal lattice or along a direction contained within a set of the lattice planes. Channeled ions are shielded from close encounters with the lattice atoms, so that the backscattered ion yield is greatly reduced. For example, the ratio of backscattered ion yield when the beam is aligned with a channeling direction to that when the beam is nonaligned (the minimum yield $\chi_{\min}$) for 3-MeV protons in silicon is about 0.03 for a $\langle 110\rangle$ crystal axis and of the order of 0.3–0.4 for $\{100\}$, $\{110\}$, and $\{111\}$ planar channeling directions.[5] The energy loss rate of channeled ions is reduced compared with that of nonchanneled (or "random") ions, as the centers of channels are regions of low electron density. The energy loss rates of MeV protons channeled in the $\{111\}$ and $\{110\}$ planes of silicon are about 0.45 and 0.60 of that of the random energy loss rate.[6] Channeled ions eventually dechannel owing to collisions with valence electrons and the thermal vibrations of the crystal atoms, and this causes them to revert to the higher, random energy loss rate. For planar channeling, the channeled fraction of the beam decreases exponentially with depth into the crystal. The dechanneling half distance (depth within which the channeled fraction is reduced by half) is about 5.0 and 4.5 μm for 3-MeV protons channeled in the $\{111\}$ and $\{110\}$ planes, respectively, of silicon.[5]

There is generally an increased probability of dechanneling if the crystal lattice is disrupted by the presence of a defect such as a dislocation or stacking fault, owing to the local displacement of atoms from their usual lattice sites. Ions dechanneled by such a defect will experience the random energy loss rate sooner than if the defect had been absent and they had been able to continue on their channeled path for longer. The mean energy loss of channeled ions transmitted through a part of a crystal containing a defect is therefore greater than that of channeled ions transmitted through a neighboring region of good crystal, and this is the basis of generating channeling images of defects using transmitted ions.

A. Effects of stacking faults on channeling

A stacking fault[7] is a planar crystal lattice defect and occurs when the regular stacking order of atomic planes

0163-1829/95/51(5)/2732(10)/$06.00

is broken by the addition or removal of a plane (forming, respectively, extrinsic or intrinsic faults). The effect of an extrinsic fault on the (111) planes of a face-centered-cubic lattice is shown in Fig. 1(a). The fault divides the crystal into two halves and can be thought of as a translation of one of the halves with respect to the other. Stacking faults are therefore described by a translation vector **R**.

Stacking faults cause dechanneling of an ion beam because the rows of atoms in one half of the crystal are moved into the channels created by those of the other half, as shown in Fig. 1(b). Without detailed consideration of the distribution of ions within the channels, the probability of a channeled ion being dechanneled by a fault is equal to the minimum yield $\chi_{\min}$ of the channeling direction being used. This is because the fault can be considered to act like a new crystal surface and will therefore dechannel a fraction of the beam equivalent to that not channeled at the crystal entrance surface.

Dechanneling by stacking faults has been well observed experimentally. α particles from a radioactive source were used[8,9] to examine thin gold foils containing stacking-fault tetrahedra. An absorber was placed between the α-particle source and the metal foil whose thickness was adjusted so that only channeled particles would be transmitted through the foil owing to their reduced energy loss rate. A collector was placed behind the metal foil which could be chemically developed to reveal the tracks of transmitted α particles. The presence of stacking-fault tetrahedra in the foil was found to significantly reduce the numbers of transmitted ions, and this was attributed to the obstruction of the channels by the displaced atomic rows. This method was used[10] to deduce values of the minimum approach distance of planar channeled α particles to the channel walls, again for stacking-fault tetrahedra in gold. A reduction in the ranges of channeled 40-keV gold ions through thin silver and gold foils containing planar defects was found from electron microscopy observations of the damage produced by the ions.[11] Backscattering has also been used to observe the dechanneling of MeV He ions by stacking faults in thin silicon layers grown epitaxially on sapphire crystals.[12] However, none of these studies produced spatially resolved information on single stacking faults. This paper demonstrates how individual faults can be imaged and characterized using ion channeling.

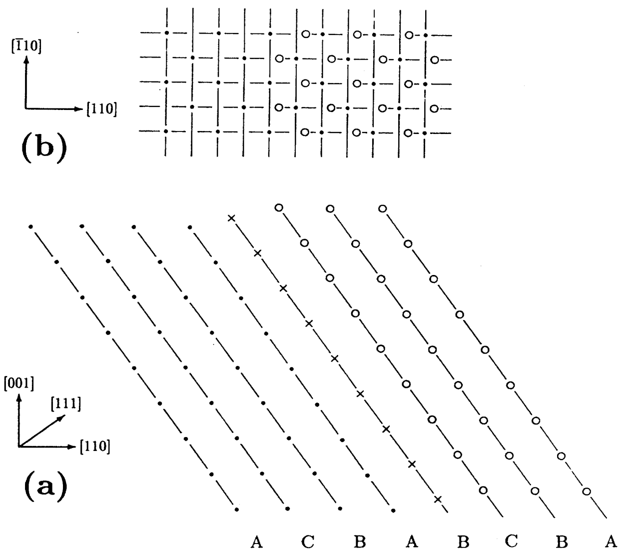

FIG. 1. Schematic showing the effect of a stacking fault on the (111) planes of a face-centered-cubic crystal. (a) Lattice projected on to the ($\bar{1}$10) plane. Atoms below the fault are solid circles, those above it are open circles, and those in the extra plane of the fault are crosses. (b) The same fault looking along the [00$\bar{1}$] crystal direction. In the fault region, rows of atoms below the fault are moved into the channels created by those above the fault. A similar diagram, for an intrinsic fault, is given in Ref. 12. It should be noted that silicon consists of two interpenetrating face-centered-cubic lattices, only one of which is shown in these diagrams for clarity.

III. EXPERIMENTAL DETAILS

Oxidation-induced stacking faults (OISF's) deliberately introduced into a silicon wafer have been used for this study of the CSTIM technique. The faults were produced by annealing the wafer in an atmosphere containing oxygen after the top, polished surface of the crystal had been damaged to produce small pits. The oxidation process injects silicon self-interstials which condense to form extrinsic stacking faults, the pits acting as sites for the fault nucleation. Such stacking faults occur on the four {111} planes of the crystal, each of which lies at an angle of 54.7° to the (001) surface plane [Fig. 2(a)]. The D-shaped faults produced in this manner all intersected the sample surface, the intersection being along [110] or [$\bar{1}$10] directions, and ran into the bulk of the silicon on one of the four {111} planes. At their lower, curved edge, they were bounded by a partial dislocation. Figure 2(b) shows schematically the appearance of faults on the four {111} planes looking along the crystal surface normal direction. It is known[13] that such OISF's have translation vectors of

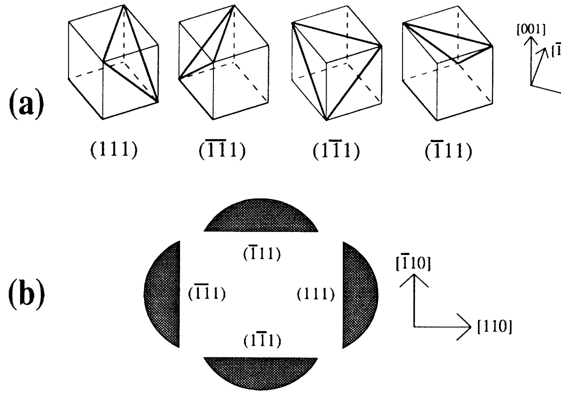

FIG. 2. (a) The four orientations of {111} planes in a cubic crystal. (b) Schematic diagram of the appearance of faults on each of the {111} plane orientations as viewed along the [00$\bar{1}$] sample surface normal direction. Faults on (111) and ($\bar{1}\bar{1}$1) planes meet the surface of the crystal along the [$\bar{1}$10] direction, and those on ($\bar{1}$11) or (1$\bar{1}$1) planes intersect the surface plane along the [110] direction.

the form $\mathbf{R}=(a/3)\langle 111\rangle$ (i.e., along the direction normal to the fault plane) equivalent to the Burgers vector of the bounding partial dislocation.

This material was prepared for CSTIM analysis by thinning it from the back, unpolished surface to a thickness of about 40 μm using wet and dry paper and then removing scratches larger than about 1 μm from this surface using diamond lapping compound.

The thinned sample was analyzed with the Oxford Nuclear Microprobe,[14] using a proton beam focused to a spot size of about 0.3×1 μm^2 with a beam divergence angle at the sample of approximately 0.04°. The use of protons rather than α particles enabled samples several tens of micrometers in thickness to be analyzed. Two different mounting configurations of goniometer and detectors were used here. Mounting 1 used a semiconductor detector positioned very close to the back of the sample and subtending a large solid angle (2.6 sr) so that virtually all the transmitted protons were detected, as described in Ref. 3. Mounting 2 used a particle detector with a restricted acceptance angle so that well-channeled protons leaving the specimen at small angles to the incident beam direction were preferentially detected and many of the less-well-channeled protons were not measured.[6] Mounting 1 allowed rotation about two axes (both orthogonal to the beam direction) so that axial channeling directions could be located, while mounting 2 allowed a greater range of tilts, but about only a single axis.

Channeling directions were located by tilting the crystal, about one or two axes for planar or axial channeling directions, respectively, until the number of protons transmitted with lower than normal energy loss was maximized. This process is described in detail in Ref. 2 and could be achieved to an angular accuracy of about 0.05° on mounting 1 and 0.03° on mounting 2. As a region of the sample was scanned by the beam, the energy spectrum of the transmitted protons was recorded at a rate of about 2000 transmitted proton energy values per second with the beam aligned with a channeling direction of the crystal, to produce an image showing the average transmitted proton energy loss in an array of 256×256 pixels. Unless otherwise stated, the images shown are printed in grey scale with darker greys representing higher energy loss. In most of the images, equal numbers of pixels were assigned to each grey level in the final image (a process called histogram equalization), spreading the energy loss values over the grey scale range and increasing the contrast in the displayed images.

IV. CSTIM RESULTS

Figure 3 is a 100-μm-wide CSTIM mean energy loss image taken with a 3-MeV proton beam channeled along the $[00\bar{1}]$ axis of the crystal. The image was taken with the sample fixed to mounting 1 so that the particle detector accepted nearly all of the transmitted protons. Periodically across the lighter grey background of the image, darker, D-shaped features can be seen. These features are stacking faults each lying on one of the four $\{111\}$ planes of the sample. Faults corresponding to each of the four types shown in Fig. 2 can be seen in the image, and they vary in length from 13 to 24 μm and in projected width from 2.5 to 3.7 μm.

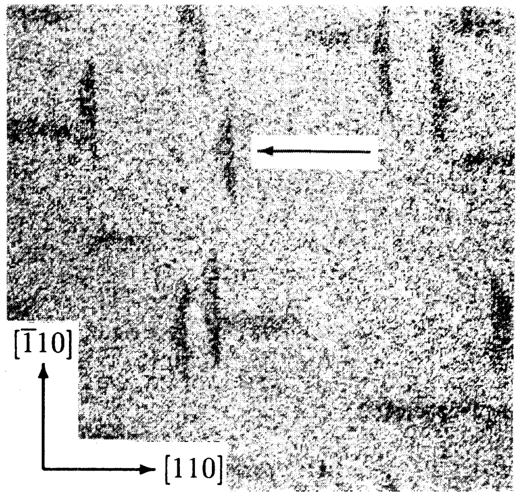

FIG. 3. 100-μm-wide CSTIM mean energy loss image of a portion of the stacking fault sample. Beam channeled along the $[00\bar{1}]$ axis.

This image was generated using 135 measured proton energy loss values per pixel. The standard deviation of the mean energy values (the image "noise level") is 8.6 ± 0.5 keV, and the most visible faults are 12 ± 2 keV above the background energy loss level. Faults meeting the surface along a line parallel to the $[\bar{1}10]$ direction of the crystal (the "vertical" faults in the image) are more clearly visible than those meeting the surface along the $[110]$ direction as the horizontal focus of the proton beam was better than the vertical.

A. Fault contrast differences between axial and planar channeling

Figure 4 shows $[00\bar{1}]$ axially channeled and (110) planar channeled images of the fault arrowed in Fig. 3. These two images are plotted over the same range of energy loss values with no histogram equalization so that the contrast can be directly compared between them. The maximum average energy loss of the fault above the background level (the fault "contrast") is 12 ± 1 keV for the axially channeled image and 22 ± 1 keV for the planar channeled image (the image noise levels are 10.5 ± 0.5 and 8.7 ± 0.5 keV for the axially and planar channeled images, respectively). The fault is more prominent in the planar channeled image because the fraction of channeled protons dechanneled at a fault is approximately given by the minimum yield for that channeling direction, which is typically 10 times higher in planar than axial alignment.[5]

B. Invisibility criterion for planar channeling

Figure 5(a) shows a CSTIM image of the same region of the sample as shown in Fig. 3, but taken with the beam channeled in the (110) planes of the sample only. It can

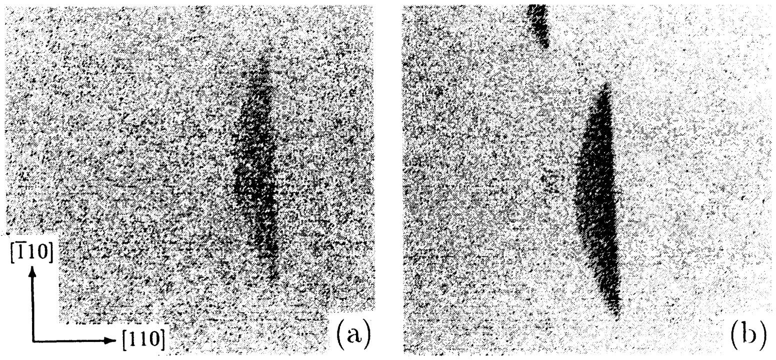

FIG. 4. 30-μm-wide CSTIM images of the fault arrowed in Fig. 3. (a) Beam axially channeled along $[00\bar{1}]$. (b) Beam planar channeled in the (110) planes.

be seen that in this image only faults which met the sample surface along the $[\bar{1}10]$ direction are visible. The faults which cannot be seen are those which were lying on the $(\bar{1}11)$ and $(1\bar{1}1)$ planes. Their invisibility in the image can be explained by noting that the translation vectors for these faults, $\mathbf{R}=(a/3)[\bar{1}11]$ and $(a/3)[1\bar{1}1]$, respectively, both lie within the (110) channeling planes. Faults with these translation vectors therefore cause no dechanneling from these planes and so are invisible in the image. Similarly, Fig. 5(b) shows the same sample region imaged with the beam channeled in the $(\bar{1}10)$ planes. Those faults with translation vectors $\mathbf{R}=(a/3)[111]$ and $(a/3)[\bar{1}\bar{1}1]$ are invisible in this case.

It is possible to produce a general criterion for the invisibility of stacking faults in ion channeling images analogous to that which exists in transmission electron microscopy (TEM) analysis. For TEM, faults are invisible in images if $\mathbf{g}\cdot\mathbf{R}=0$, ±1, ±2, etc., where $\mathbf{g}$ is the reciprocal lattice vector corresponding to the reflecting planes and $\mathbf{R}$ is the fault vector.[13] $\mathbf{g}\cdot\mathbf{R}=0$ implies that the fault vector is contained within the reflecting planes, and so no contrast is observed. Invisibility for $\mathbf{g}\cdot\mathbf{R}=\pm1$, ±2, etc., arises because addition of a lattice vector to the fault vector does not affect the contrast (in the terms used to describe stacking faults above, a translation of the crystal by a lattice vector does not displace atomic rows into channels) and the dot product of $\mathbf{R}$ with a lattice vector is an integer. For example, a translation vector $\mathbf{R}=(a/3)[111]$ is equivalent (as far as displacement of rows into channels) to a vector $\mathbf{R}=(a/6)[2\bar{1}\bar{1}]$ because

$$\frac{a}{3}[111]=\frac{a}{6}[2\bar{1}\bar{1}]+\frac{a}{2}[011]$$

and $(a/2)[011]$ is a lattice vector.

In channeling, the same $\mathbf{g}\cdot\mathbf{R}$ criterion can be used to predict the faults that will be invisible for channeling in a given set of planes, although care must be taken to use the correct $\mathbf{g}$ vector. The channeling planes used to produce the two images of Fig. 5 were described as (110) and $(\bar{1}10)$, as plane indices are reduced to the lowest form possible. However, the reciprocal lattice vectors for these planes are [220] and $[\bar{2}20]$, respectively, and it is these vectors that must be used when calculating $\mathbf{g}\cdot\mathbf{R}$. This is because the use of [220] and $[\bar{2}20]$ correctly takes into account the interplanar spacing, which is $a/2\sqrt{2}$ in face-centered-cubic crystals and not $a/\sqrt{2}$ as it is in simple cubic crystals. (This is analogous to TEM analysis of silicon crystals, where reflections with $\mathbf{g}=\langle 110\rangle$ are forbidden and $\mathbf{g}=\langle 220\rangle$ is the correct vector.) For example, in Fig. 5(b), the faults on the (111) planes, with fault vector $(a/3)[111]$, are invisible. In this case, $\mathbf{g}\cdot\mathbf{R}$ is calculated from $[\bar{2}20]\cdot(a/3)[111]=0$. Equivalently, with the fault vector represented by $(1/6)[2\bar{1}\bar{1}]$, $\mathbf{g}\cdot\mathbf{R}=-1$. This demonstrates that, as in TEM, $\mathbf{g}\cdot\mathbf{R}$ equal to zero or an integer produces invisibility; the disappearance of faults on the $(\bar{1}11)$, $(1\bar{1}1)$, and $(\bar{1}\bar{1}1)$ planes in the images of Fig. 5 can be similarly explained.

The crystal was fixed to mounting 2 so that other channeling planes could be reached It was mounted so that the [010] direction ran approximately horizontally and the [100] direction nearly parallel to the vertical rotation axis, and a particle detector with an acceptance half-angle of ~0.4° was used.

Figure 6(a) is a stereographic projection of the sample in this orientation, and marked is the angular path of the beam as the sample was tilted. At a tilt angle of about −45° the beam was close to the $[0\bar{1}1]$ crystal axis and could be aligned with the $(\bar{1}11)$, (011), or (111) planes

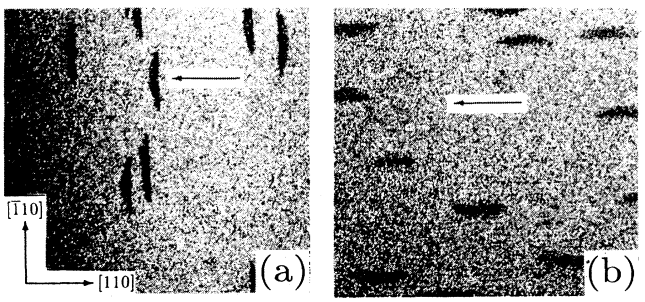

FIG. 5. The same region of the sample as Fig. 3, but with the beam channeled in the (a) (110) and (b) $(\bar{1}10)$ planes. The same fault is arrowed in Figs. 3 and (a), and in (b) the arrow points to the fault's position if it had been visible.

which intersect at this axis. With the beam near the crystal [001] axis (close to zero tilt angle), the $(\bar{1}10)$, (010), or (110) planes could be used for channeling. When the sample was tilted through approximately $+45°$ so that the beam was near the [011] axis, the $(1\bar{1}1)$, $(0\bar{1}1)$, and $(\bar{1}\bar{1}1)$ planes were accessible.

Figure 6(b) shows the mean transmitted proton energy as a function of sample tilt angle, obtained by recording a series of transmitted proton energy spectra. This curve has been plotted with the (010) channeling direction at zero tilt angle. The mean energy decreases as the tilt angle θ was increased from 0° owing to the effective increase in sample thickness of $t/\cos\theta$ μm where t was about 40 μm. However, the mean transmitted energy was increased every time the beam was aligned with one of the nine planar channeling directions listed above. Channeling in $\{111\}$ planes produced the largest increase in mean transmitted energy, followed by channeling in $\{110\}$ planes, with the (010) plane producing the smallest energy increase. This is because on going from $\{111\}$ to $\{110\}$ to $\{100\}$ channeling, the ratio of channeled to random energy loss increases. The $\{111\}$ planes also have a slightly greater dechanneling half distance than the $\{110\}$ planes.

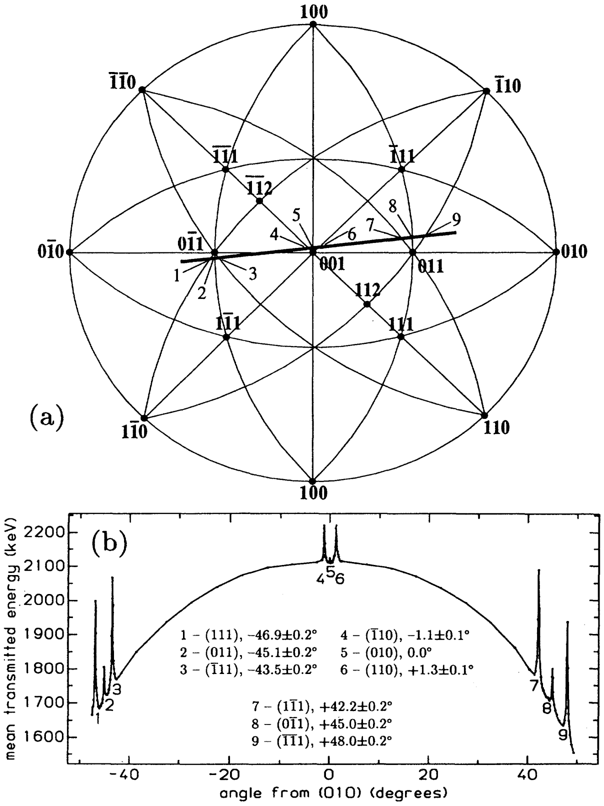

FIG. 6. (a) [001] stereographic projection showing the major planes referred to in the text. (b) Mean energy loss of 3-MeV protons passing through a 40-μm-thick crystal vs angle from the (010) planar channeling direction for the angular path of the beam shown by the dark line in (a). The peaks in the curve occurred when the beam was aligned with planar channeling directions, and the numbers with which they are labeled correspond to the positions on the stereographic projection in (a). The curve was produced by recording transmitted proton energy spectra at intervals over the angular range and calculating the mean energy loss from each spectrum. The points were taken at 5° intervals away from the major channeling directions and at intervals of between 0.025° and 0.1° close to channeling alignment. They have been joined by straight lines to show the shape of the curve more clearly. The angular distance of each peak from the (010) channeling direction is given.

Figure 7 shows CSTIM images taken with the beam aligned with each of the nine major planar channeling directions shown in Fig. 6(b). Figure 7(a), 7(b), and 7(c) were taken with the beam close to zero tilt angle at positions 6, 5, and 4, respectively, on the stereographic projection so that the beam was channeled in each of the (110), (010), and $(\bar{1}10)$ planes. In each of the (110) and $(\bar{1}10)$ channeled images, two of the four types of fault are invisible as for Figs. 5(a) and 5(b). In the (010) channeled image, faults with all four possible translation vectors can be seen as none have $\mathbf{g}\cdot\mathbf{R}$ equal to an integer. In an image taken with the beam $+0.44°$ from (010) channeling (therefore beam effectively not channeled), between the angles for (010) and (110) channeling, no faults could be seen (image not shown). This demonstrates that for images when faults could be seen, they were visible owing to channeling contrast and not because of local variations in sample thickness at the faults. In addition, it shows that the appearance of all four types of fault in the (010) channeled image was genuinely caused by (010) channeling and not from an overlap of channeling effects from the nearby (in angle) (110) and $(\bar{1}10)$ planes.

The images shown in Figs. 7(d), 7(e), and 7(f) were, respectively, taken at positions 1, 2, and 3 on the stereographic projection with the beam channeled in the (111), (011), and $(\bar{1}11)$ planes. In Fig. 7(d), faults on the (111) and $(\bar{1}11)$ planes cannot be seen. The reason for this is that faults on the (111) planes are end on in the image and those on the $(\bar{1}11)$ planes were almost end on, as the beam was about 3.4° from the $(\bar{1}11)$ channeling direction. The narrow line that would have been the image of these faults cannot be seen on this relatively large area scan owing to the image noise level. The image of Fig. 7(f), with the beam $(\bar{1}11)$ channeled, is similar; in this case, the $(\bar{1}11)$ faults are end on and the (111) faults are almost end on, so that neither of these types can be seen. No faults at all can be seen in the (011) channeled image [Fig. 7(e)]. This is because the (111) and $(\bar{1}11)$ faults were nearly end on and so again cannot be seen. Faults on the $(1\bar{1}1)$ and $(\bar{1}\bar{1}1)$ planes have $\mathbf{g}\cdot\mathbf{R}=0$ and so are also invisible. The image of Fig. 7(e) was taken with the beam less than 2° from the images of Figs. 7(d) and 7(f), so that the $(1\bar{1}1)$ and $(\bar{1}\bar{1}1)$ faults were not close to end on.

The images of Figs. 7(g), 7(h), and 7(i) were taken at positions 7, 8, and 9 on the stereographic projection with the beam channeled in the $(1\bar{1}1)$, $(0\bar{1}1)$, and $(\bar{1}\bar{1}1)$ planes, respectively. For all three images, the $(1\bar{1}1)$ and $(\bar{1}\bar{1}1)$ faults were either end on or close to end on and so cannot be seen [although in Fig. 7(g) $(\bar{1}\bar{1}1)$ faults can just be seen as straight, dark lines]. In Fig. 7(h), the (111) and $(\bar{1}11)$

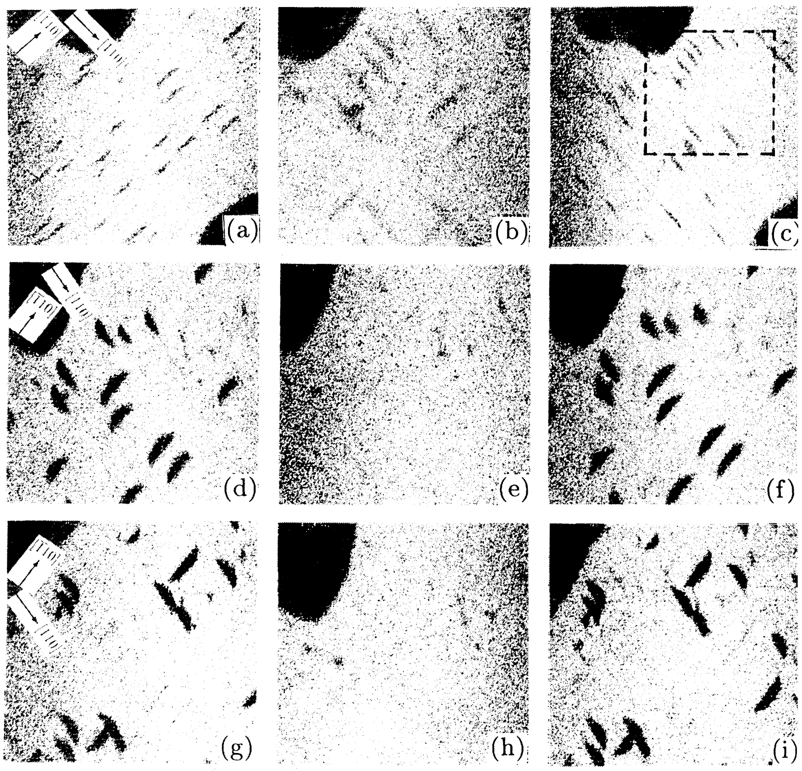

FIG. 7. CSTIM images taken with the beam aligned with nine planar channeling directions. The position numbers refer to Fig. 6. (a) 200 μm wide, (110) (position 6), (b) 100 μm wide, (010) (position 5), (c) 200 μm wide, $(\bar{1}10)$ (position 4), (d) 125 μm wide, (111) (position 1), (e) 125 μm wide, (011) (position 2), (f) 125 μm wide, $(\bar{1}11)$ (position 3), (g) 125 μm wide, $(1\bar{1}1)$ (position 7), (h) 125 μm wide, $(0\bar{1}1)$ (position 8), and (i) 125 μm wide, $(\bar{1}\bar{1}1)$ (position 9). Owing to the sample tilt angle of approximately 45° in images (d)–(i), the actual area of the sample surface scanned by the beam was 177×125 μm^2. The region surrounded by a dashed line in (c) is approximately the region imaged in (b) and (d)–(i).

faults have $\mathbf{g}\cdot\mathbf{R}=0$ and so they are also invisible.

The effect of faults being close to end on can be seen from the images of Fig. 8. Figure 8(a) was taken with the beam channeled in the (111) planes as for Fig. 7(d), but with the beam close to the $[\bar{1}\,\bar{1}2]$ crystal axis rather than the $[0\bar{1}1]$ axis. In this orientation, faults on the $(\bar{1}11)$ planes are clearly visible (and two are arrowed), whereas they could not be seen in Fig. 7(d) owing to them being close to end on. Similarly, Fig. 8(b) was taken with the beam channeled in the $(\bar{1}\,\bar{1}1)$ planes as for Fig. 7(i), but close to the [112] crystal axis rather than the [011] axis. Faults on $(1\bar{1}1)$ planes are visible in Fig. 8(b) (and the arrow head is between two such faults), as they are no longer close to end on as they were for Fig. 7(i).

Table I gives a summary of the 11 CSTIM images presented in Figs. 7 and 8. For each image, an approximate value of the contrast of the visible faults is given, where the fault contrast is defined as the difference in mean energy loss between the faults and the image background. It can be seen that the contrast was affected by choice of channeling direction, with {111} planes producing the strongest contrast in the faults that were visible, followed by {110} planes, and with the (010) planar direction producing the weakest contrast. This is due to the fact that the {111} planes have the lowest ratio of channeled to random energy loss and the longest dechanneling half distance. The amount of dechanneling caused by the faults from {111} and {110} planes is likely to be very similar: Both types of planes have similar measured values for the fraction of protons that are initially channeled (minimum yield) and the displacement of the planes below a fault into the channels formed by those above it is equal to one-third of the interplanar distance in both cases. A future paper will discuss in more detail factors

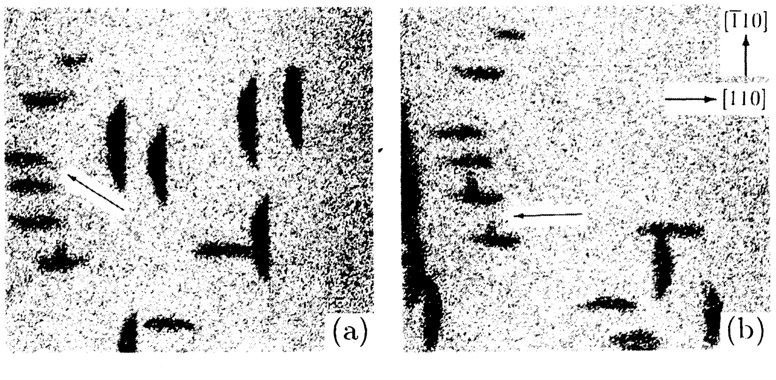

FIG. 8. 100-μm-wide CSTIM images of the region of the sample shown in Fig. 7. (a) Beam channeled in the (111) planes, close to the $[\bar{1}\,\bar{1}2]$ crystal axis. (b) Beam channeled in the $(\bar{1}\,\bar{1}1)$ planes, close to the [112] crystal axis.

TABLE I. Summary of the invisibility of stacking faults in the images of Figs. 7 and 8. Also given for each channeling direction is the fault contrast and noise level in the image. NA in the contrast column means that no faults were visible in the image so that a contrast value is not applicable.

Channeling direction	Figure number	Contrast of visible faults (keV)	Noise (keV)	Invisible faults	Reason for invisibility
(010)	7(b)	4.6±0.7	4.9	none	
(110)	7(a)	24±4	15	$(\bar{1}11)$	$\mathbf{g}\cdot\mathbf{R}=0$
				$(1\bar{1}1)$	$\mathbf{g}\cdot\mathbf{R}=0$
$(\bar{1}10)$	7(c)	28±6	17	(111)	$\mathbf{g}\cdot\mathbf{R}=0$
				$(\bar{1}\bar{1}1)$	$\mathbf{g}\cdot\mathbf{R}=0$
(011)	7(e)	NA	15	$(1\bar{1}1)$	$\mathbf{g}\cdot\mathbf{R}=0$
				$(\bar{1}\bar{1}1)$	$\mathbf{g}\cdot\mathbf{R}=0$
				$(\bar{1}11)$	nearly end on
				(111)	nearly end on
$(0\bar{1}1)$	7(h)	NA	15	$(\bar{1}11)$	$\mathbf{g}\cdot\mathbf{R}=0$
				(111)	$\mathbf{g}\cdot\mathbf{R}=0$
				$(1\bar{1}1)$	nearly end on
				$(\bar{1}\bar{1}1)$	nearly end on
(111)	7(d)	93±9	32	(111)	end on
				$(\bar{1}11)$	nearly end on
(111)	8(a)	86±9	25	(111)	end on
$(\bar{1}11)$	7(f)	118±23	28	$(\bar{1}11)$	end on
				(111)	nearly end on
$(1\bar{1}1)$	7(g)	123±16	28	$(1\bar{1}1)$	end on
				$(\bar{1}\bar{1}1)$	nearly end on
$(\bar{1}\bar{1}1)$	7(i)	127±18	31	$(\bar{1}\bar{1}1)$	end on
				$(1\bar{1}1)$	nearly end on
$(\bar{1}\bar{1}1)$	8(b)	106±10	35	$(\bar{1}\bar{1}1)$	end on
none	not shown	NA	5.3	all	no channeling

affecting CSTIM image contrast, which is also determined by the amount of detector collimation, sample thickness, and beam divergence.

For each image, the standard deviation of the energy loss values in each image is given (the "noise" on the image). The noise level was determined by factors such as the choice of channeling direction and the sample thickness, which affect the width of the distribution of proton energy values at each pixel, and the length of time that the image was collected for. The levels for {111} channeled images are in general the largest, followed by those of {110} channeled images, with the lowest noise level being for the (010) and nonchanneled images. This is primarily caused by the greater width of the transmitted proton energy spectrum for {111} channeling. Collecting the images for longer would have reduced the noise level and enabled any fainter features present to be seen. Also listed in the table are the faults that were invisible in each image and the reason for their invisibility.

From the images above, it can be seen that CSTIM has the ability to determine the direction of the translation vector of stacking faults. For example, it has been shown [Figs. 7(c) and 7(h)] that faults on the (111) planes were invisible for channeling in the $(\bar{1}10)$ and $(0\bar{1}1)$ planes. The fault vector of the (111) faults must therefore be perpendicular to the $[\bar{1}10]$ and $[0\bar{1}1]$ directions, which means **R** consists of a vector along [111] (plus an arbitrary lattice vector).

C. Contrast across a fault

In the image of Fig. 4(b), which was taken within 0.05° of the (110) planar channeling direction with an uncollimated detector, part of the fault closest to the sample surface (the straight edge) is showing stronger contrast than deeper parts of the fault. Figure 9(a) shows a plot of the fault contrast versus distance across the center of the fault, from which it is possible to measure accurately the width of the fault and hence its depth at its deepest point. The width, measured from the midpoints of the left and right sides, is 3.0±0.2 μm, so that the deepest part of the fault was $3\times\tan 54.7°=4.2\pm0.3$ μm below the sample surface.

The contrast across the fault decreases on going from the part of the fault at the sample surface (right-hand side of the fault) to the deeper part (left-hand side). This is caused by the decrease in the fraction of the protons that are channeled with depth in the crystal owing to "natural" dechanneling. At a depth of about 4.2 μm into the sample, almost half of the protons channeled at the sample surface have been dechanneled. There are therefore 50% fewer protons to be dechanneled by the fault at its deepest point than close to the sample surface, and so the contrast is lower for the deeper parts of the fault. Those protons dechanneled at a depth of 4 μm have traveled this distance with the reduced energy loss rate, and this also lowers the contrast from deeper parts of the fault.

From the rate of decrease of the fault contrast in Fig. 9(a), it is expected that faults of the order of 10 μm below the sample surface would be detectable by CSTIM when 3-MeV protons channeled in $\{110\}$ planes and an uncollimated detector are used.

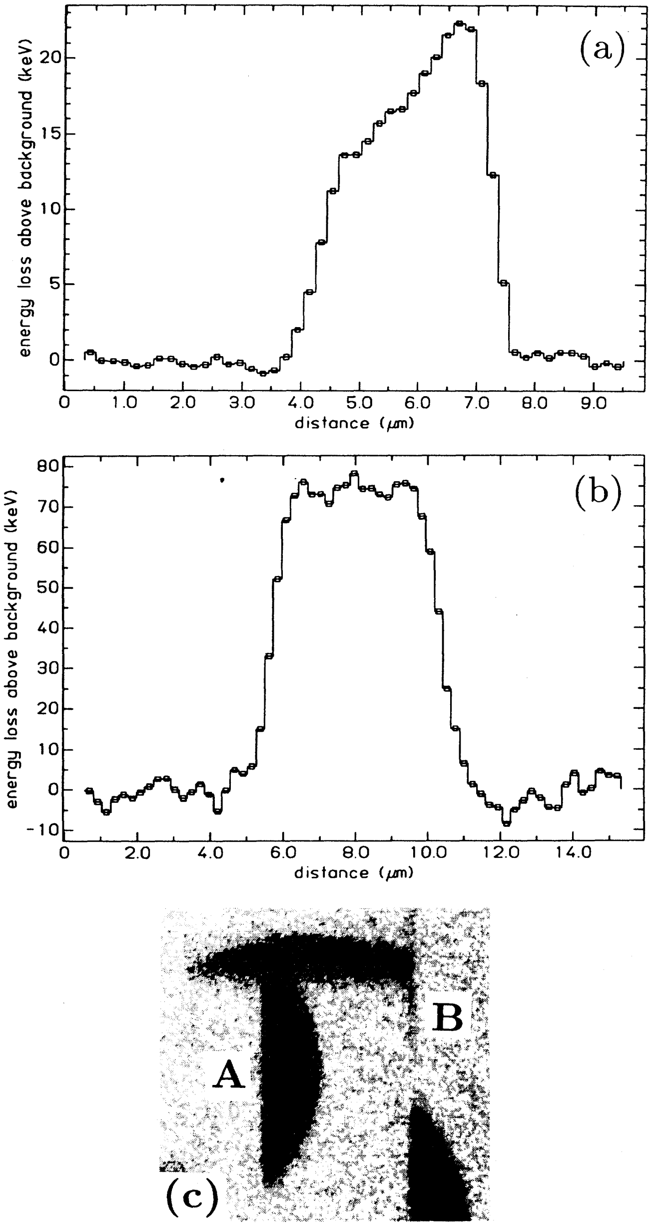

FIG. 9. (a) Line scan across the fault shown in Fig. 4(b) taken with the beam channeled in the (110) planes and a large acceptance angle detector used. The background has been subtracted to show the fault contrast as a function of distance across the fault. Each point has been smoothed with those 0.2 μm on either side of it. Right-hand side of the fault closest to the sample surface. (b) Line scan across the fault labeled A in (c). Left-hand side of the fault closest to the sample surface. (c) 30-μm-wide CSTIM image taken with the beam channeled in the $(\bar{1}\bar{1}1)$ planes showing a fault on a (111) plane (A) and an end on fault on a $(\bar{1}\bar{1}1)$ plane (B).

An error function fitted to the right-hand side of the fault feature revealed that the full width at half maximum (FWHM) of beam spot size when this line scan was taken was 0.45 ± 0.03 μm (assuming it to have been a Gaussian). A similar fit to the left-hand, deeper side of the fault revealed that a Gaussian of FWHM 0.75 ± 0.07 μm would have been required to produce the shape of this side of the fault. This larger width at the deeper part of the fault was possibly caused by the effects on channeling of the bounding partial dislocation (the beam spot size would not have increased by more than 0.05 μm in the top 4.2 μm of the sample[15]).

The depth of the deepest fault detectable using transmission ion channeling is of interest. It is probable that CSTIM can produce images of faults deeper than 10 μm when a collimated detector is used and when the channeling direction is $\{111\}$. Figure 9(b) shows the contrast across a fault on a (111) plane [shown in Fig. 9(c)] taken with the beam channeled in the $(\bar{1}\bar{1}1)$ planes and with a detector collimated to an acceptance half-angle of $\sim 1°$. The contrast of the fault, about 75 keV, is very much larger than the 22-keV contrast shown by the part of the fault closest to the sample surface in Fig. 9(a) for two reasons. As discussed previously, the channeling direction used for the image affects the contrast, with $\{111\}$ producing stronger contrast than $\{110\}$. Additional, many of the protons that were not initially channeled were not collected in the restricted acceptance angle detector, which can also increase the fault contrast in CSTIM images While measurement times of tens of minutes were required before faults became visible using an uncollimated detector with a $\{110\}$ channeling direction, when a collimated detector and $\{111\}$ channeling were used faults could be observed after just 1 min of data collection.

From Fig. 9(b), the width of the fault as seen by the beam was 4.7 ± 0.3 μm. Using this width, it can be shown using simple geometry that the deepest part of the fault as viewed by the beam in this sample orientation (i.e., with the beam at 35.3° to the sample surface normal direction) was 5.0 ± 0.3 μm below the sample surface, for the right-hand side of the fault. However, there is very little falloff in contrast between the part of the fault at the sample surface (left-hand side of the fault) and the deepest part. In comparison, the fault contrast decreased with depth in Fig. 9(a). It is believed that the use of a restricted acceptance angle detector in excluding many of the nonchanneled particles and use of a $\{111\}$ channeling direction (with a larger dechanneling half thickness than $\{110\}$) meant that the contrast of a fault decreased less rapidly with depth into the sample. Preferential detection of channeled protons and choice of channeling direction should enable faults deeper than 10 μm to be imaged with this technique.

Also visible in the image of Fig. 9(c) is a thin dark line running vertically near the top right of the image (labeled B). This was caused by a fault on the $(\bar{1}\bar{1}1)$ planes which was end on in the image. It is unlikely that the dechanneling produced by this fault was caused by the extra fault plane itself: This would have appeared to the beam as any other $(\bar{1}\bar{1}1)$ plane, and indeed $\mathbf{g}\cdot\mathbf{R}$ is an integer for

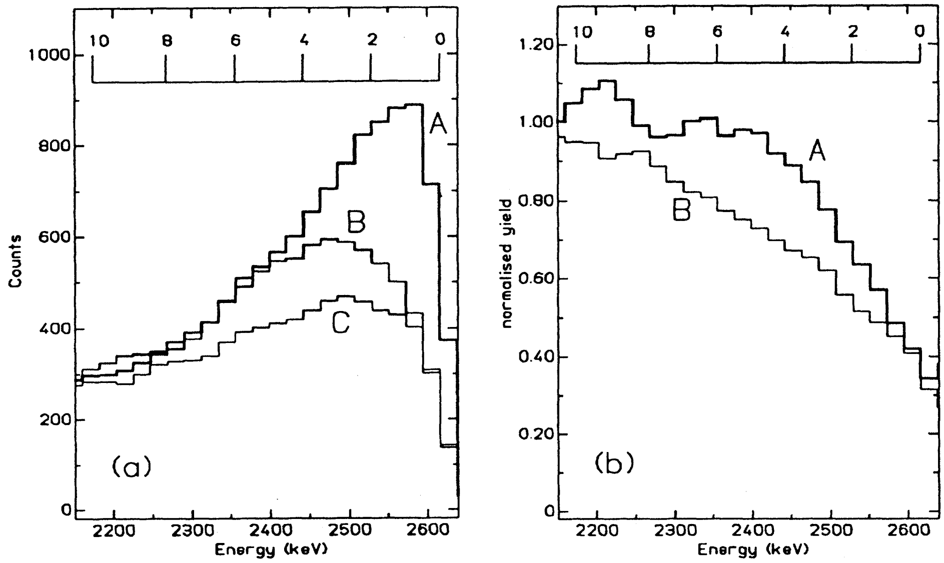

FIG. 10. (a) Backscattered proton spectra taken from the stacking fault sample. A depth scale in micrometers, assuming nonchanneled energy loss rate, is given at the top of the plot. A, random spectrum. B and C, beam aligned with the $(\bar{1}\bar{1}1)$ planes, but B with the beam scanning only stacking faults and C with the beam scanning virgin crystal. (b) A, ratio of the spectrum taken on the faults to the random spectrum. B, ratio of the spectrum from virgin crystal to the random spectrum.

this fault with this channeling direction. However, where the fault ended inside the crystal, the lattice planes would have been locally distorted by the partial dislocation bounding the fault plane. It is therefore believed that the end on fault is visible because of the dechanneling produced by the partial dislocation.

V. BACKSCATTERING ANALYSIS

It has been demonstrated that images of individual stacking faults can be produced by transmission ion channeling. It is of interest to examine whether backscattered ion channeling could also be used for stacking fault analysis.

A group of six stacking faults which were lying either on (111) or $(\bar{1}11)$ planes was located by transmission channeling using a 3-MeV proton beam channeled in the $(\bar{1}\bar{1}1)$ planes. The beam current was then increased to that required for backscattering spectrometry—about 80×10^{-12} A (equivalent to 5×10^{8} protons per second or six orders of magnitude greater than the current used in transmission with an uncollimated detector). The $(\bar{1}\bar{1}1)$ channeled beam was set to scan only over the fault region of the sample, and a backscattered proton energy spectrum was recorded. A backscattered ion detector located at an angle of 155° to the incident beam direction and subtending a solid angle of 80 msr was used. Similar spectra were recorded with the beam channeled, but scanning unfaulted (virgin) crystal and with the beam not channeled (a "random" spectrum). These three spectra are shown in Fig. 10(a). The total dose delivered to the sample when the beam was scanning just the fault regions was about 1×10^{17} protons per cm^2. This is of the order of the dose required to produce detectable lattice damage in the sample.[16] Backscattering analysis of individual faults is limited by the fact that small areas of the sample would receive high beam doses, and sample lattice damage becomes a significant problem. This is why the beam was set to scan over six faults rather than a single fault.

In Fig. 10(b), the ratios of the two channeled spectra (on and off the faults) to the random spectra are shown. No correction has been made in the ratio plots for the difference in energy loss rate between channeled and random protons. These ratio curves show the following. First, the ratio of the channeled spectra to the random spectrum at the sample surface is 0.35 ± 0.05, which is the minimum yield for this channeling direction. This ratio increases slowly for the channeled spectrum from the virgin crystal, reaching 0.95 at a depth of the about 10 μm into the sample. It is therefore unlikely that backscattering will be sensitive to faults deeper than about 10 μm (for 3-MeV protons) owing to the natural dechanneling of the beam.

The ratio of the spectrum taken on the faulted region to the random spectrum increases much more rapidly with depth than the virgin/random ratio. This is because of the dechanneling produced by the faults, which ran from the sample surface to a depth of about 5 μm. Virtually all of the protons had been dechanneled by this depth with the beam scanning the faults.

VI. CONCLUSIONS

It has been demonstrated that ion channeling can be used to produce images of stacking faults that are at least 10 μm below the sample surface in silicon crystals that are tens of micrometers in thickness. The observed fault contrast is affected by the choice of channeling direction. Planar channeling can be used to give information on the stacking-fault translation vector, although care must be taken to distinguish between faults that are close to end on and those for which $\mathbf{g}\cdot\mathbf{R}$ is equal to zero or an integer. The spatial resolution of the technique is presently limited to a few tenths of a micrometer by the size of the proton beam spot. It should be noted that, while the technique of TEM has a significantly better spatial resolution than CSTIM, it requires samples that are generally less than 1 μm in thickness (up to a few micrometers in thickness for high-voltage TEM's) and so would be unable to produce images showing faults in this crystal throughout their depth. X-ray topography can image stacking faults in bulk crystals, but with poorer spatial resolution than CSTIM. The scanning electron microscope provides the technique of electron-beam-induced current (EBIC) which can image stacking faults in bulk specimens with a spatial resolution of about 1 μm, but with strong contrast only if the faults are decorated with metal impurity atoms and with no information on the fault vector. CSTIM seems to complement these techniques by being able to image faults several micrometers below a sample surface with submicrometer spatial resolution and with the ability to give information on stacking-fault translation vectors. In principle, channeling contrast backscattered ion images of stacking faults could be produced and $\mathbf{g}\cdot\mathbf{R}$ analysis performed as demonstrated for the transmitted ion case. Backscattering analysis does not require the sample to be thinned and can produce depth-resolved information (the ability of the transmitted ion technique to produce depth-resolved information still remains to be demonstrated). However, the high beam doses required to produce backscattered ion images are likely to be prohibitive.

Computer simulations of the interaction of channeled ions with stacking faults and other crystal defects have been performed to complement the experimental CSTIM results, and these will be published in future papers.

ACKNOWLEDGMENTS

P.J.C.K. and P.R.W. would respectively like to thank the Royal Commission for the Exhibition of 1851 and the Royal Society for financial support. Thanks are due to Dr. R. Falster of Monsanto Electronic Materials Corporation for providing the stacking fault sample and to Dr. G.R. Booker for useful discussions on the fault invisibility criterion.

---

[1] L. C. Feldman, J. W. Mayer, and S. T. Picraux, *Materials Analysis by Ion Channeling* (Academic, New York, 1982).

[2] M. B. H. Breese, P. J. C. King, J. Whitehurst, G. R. Booker, G. W. Grime, F. Watt, L. T. Romano, and E. H. C. Parker, J. Appl. Phys. **73**, 2640 (1993).

[3] P. J. C. King, M. B. H. Breese, G. R. Booker, J. Whitehurst, P. R. Wilshaw, G. W. Grime, F. Watt, and M. J. Goringe, Nucl. Instrum. Methods B **77**, 320 (1993).

[4] P. J. C. King, M. B. H. Breese, P. R. Wilshaw, G. R. Booker, G. W. Grime, F. Watt, and M. J. Goringe, in *Microscopy of Semiconducting Materials 1993,* Proceedings of the Royal Microscopical Society Conference, Oxford, edited by A. G. Cullis, A. E. Staton-Bevan, and J. L. Hutchison, IOP Conf. Proc. No. 134 (Institute of Physics and Physical Society, London, 1993), p. 153.

[5] J. A. Davies, J. Denhartog, and J. L. Whitton, Phys. Rev. **165**, 345 (1968).

[6] B. R. Appleton, C. Erginsoy, and W. M. Gibson, Phys. Rev. **161**, 330 (1967).

[7] D. Hull, *Introduction to Dislocations* (Pergamon, Oxford, 1975).

[8] Y. Quéré, J.-C. Resneau, and J. Mory, C. R. Acad. Sci. Paris B **262**, 1528 (1966).

[9] Y. Quéré and H. Couve, J. Appl. Phys. **39**, 4012 (1968).

[10] J. Mory and Y. Quéré, Radiat. Eff. **13**, 57 (1972).

[11] T. Schober and R. W. Baluffi, Phys. Status Solidi **27**, 195 (1968).

[12] S. U. Campisano, G. Foti, E. Rimini, and S. T. Picraux, Nucl. Instrum. Methods **149**, 371 (1978).

[13] G. R. Booker and W. J. Tunstall, Philos. Mag. **13**, 71 (1966).

[14] G. W. Grime, M. Dawson, M. Marsh, I. C. McArthur, and F. Watt, Nucl. Instrum. Methods B **54**, 52 (1991).

[15] J. P. Biersack and L. G. Haggmark, Nucl. Instrum. Methods **174**, 257 (1980).

[16] P. J. C. King, Ph. D. thesis, University of Oxford, 1993.

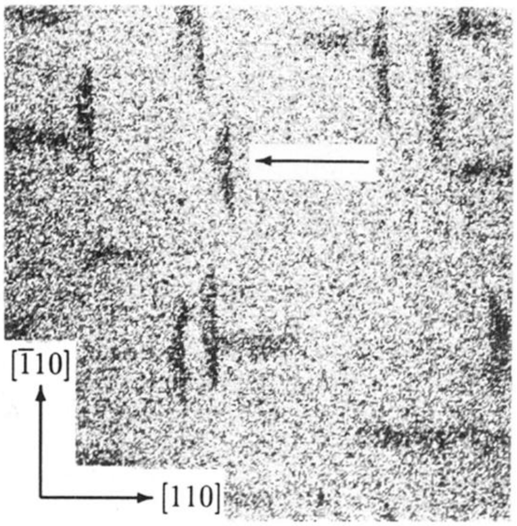

FIG. 3. 100-μm-wide CSTIM mean energy loss image of a portion of the stacking fault sample. Beam channeled along the [$00\bar{1}$] axis.

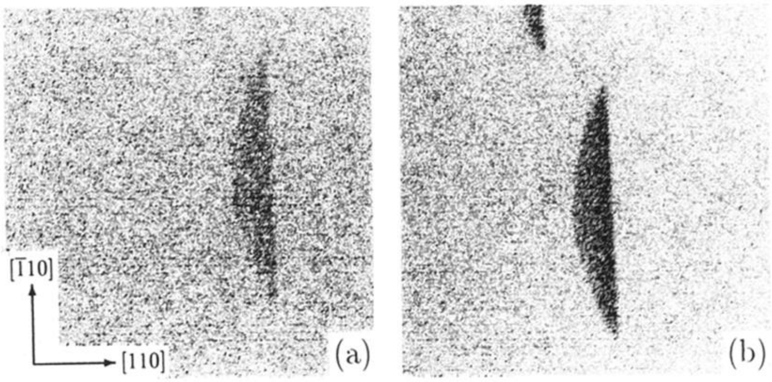

FIG. 4. 30-μm-wide CSTIM images of the fault arrowed in Fig. 3. (a) Beam axially channeled along [00$\bar{1}$]. (b) Beam planar channeled in the (110) planes.

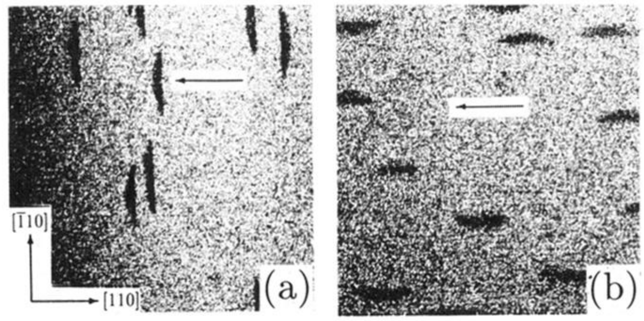

FIG. 5. The same region of the sample as Fig. 3, but with the beam channeled in the (a) (110) and (b) ($\bar{1}$10) planes. The same fault is arrowed in Figs. 3 and (a), and in (b) the arrow points to the fault's position if it had been visible.

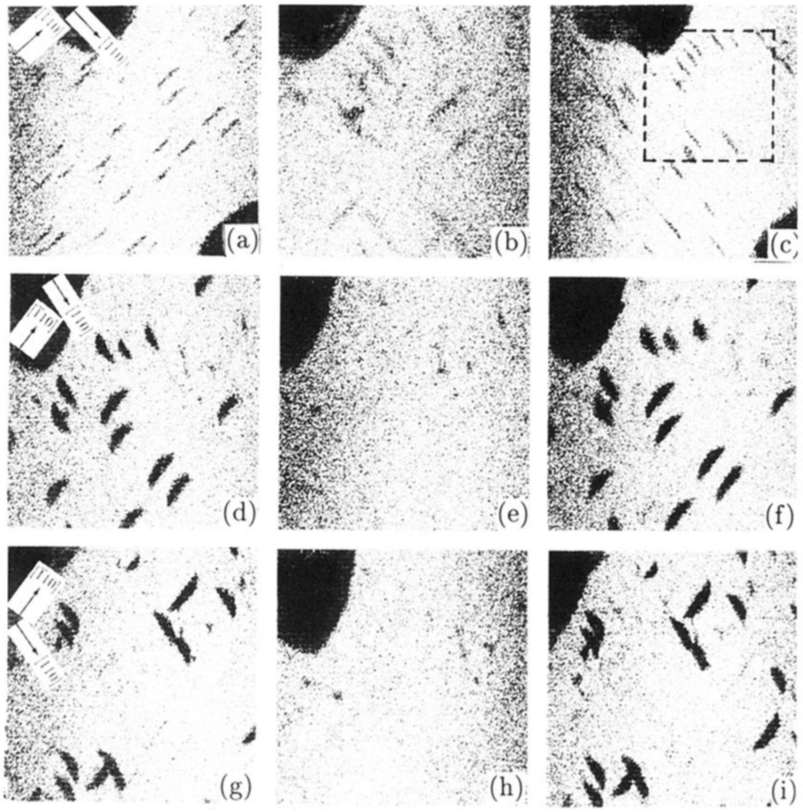

FIG. 7. CSTIM images taken with the beam aligned with nine planar channeling directions. The position numbers refer to Fig. 6. (a) 200 μm wide, (110) (position 6), (b) 100 μm wide, (010) (position 5), (c) 200 μm wide, $(\bar{1}10)$ (position 4), (d) 125 μm wide, (111) (position 1), (e) 125 μm wide, (011) (position 2), (f) 125 μm wide, $(\bar{1}11)$ (position 3), (g) 125 μm wide, $(1\bar{1}1)$ (position 7), (h) 125 μm wide, $(0\bar{1}1)$ (position 8), and (i) 125 μm wide, $(\bar{1}\bar{1}1)$ (position 9). Owing to the sample tilt angle of approximately 45° in images (d)–(i), the actual area of the sample surface scanned by the beam was $177\times125\ \mu\text{m}^2$. The region surrounded by a dashed line in (c) is approximately the region imaged in (b) and (d)–(i).

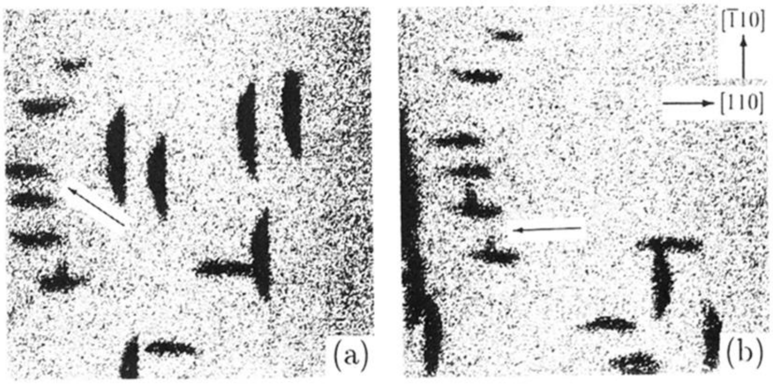

FIG. 8. 100-μm-wide CSTIM images of the region of the sample shown in Fig. 7. (a) Beam channeled in the (111) planes, close to the [$\bar{1}\,\bar{1}$2] crystal axis. (b) Beam channeled in the ($\bar{1}\,\bar{1}$1) planes, close to the [112] crystal axis.

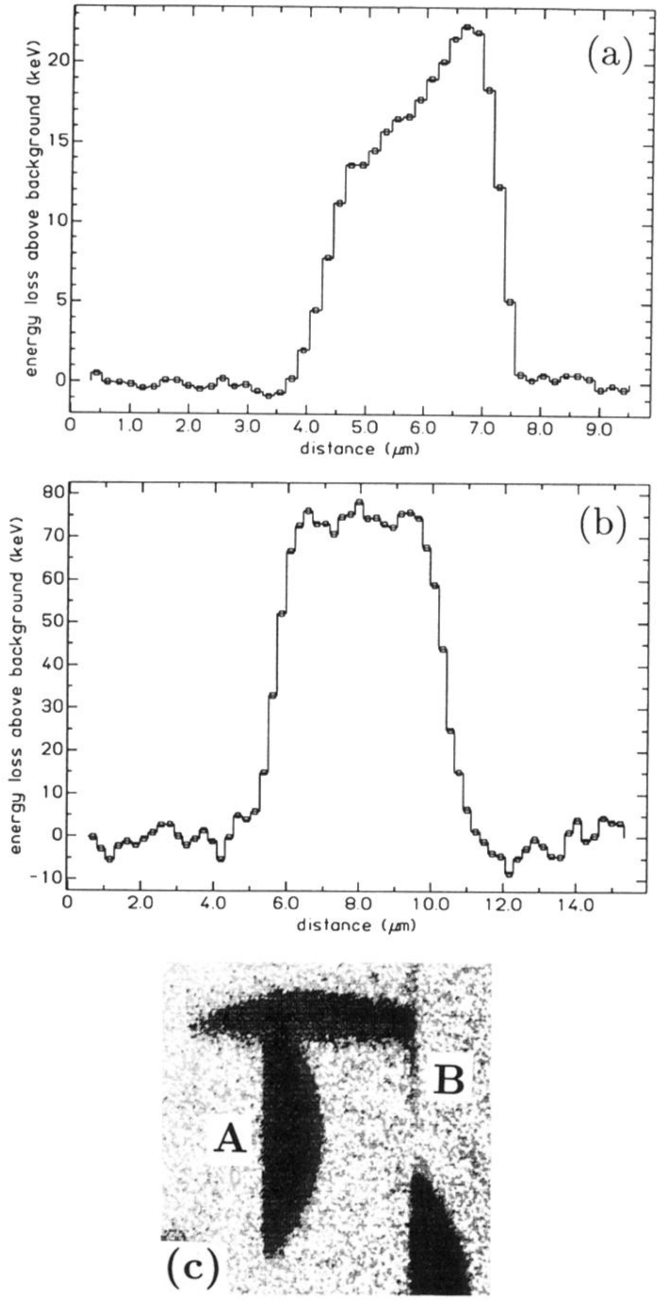

FIG. 9. (a) Line scan across the fault shown in Fig. 4(b) taken with the beam channeled in the (110) planes and a large acceptance angle detector used. The background has been subtracted to show the fault contrast as a function of distance across the fault. Each point has been smoothed with those 0.2 μm on either side of it. Right-hand side of the fault closest to the sample surface. (b) Line scan across the fault labeled A in (c). Left-hand side of the fault closest to the sample surface. (c) 30-μm-wide CSTIM image taken with the beam channeled in the $(\bar{1}\bar{1}1)$ planes showing a fault on a (111) plane (A) and an end on fault on a $(\bar{1}\bar{1}1)$ plane (B).